Large-Size Free-Standing Single-crystal β-Ga₂O₃ Membranes Fabricated by Hydrogen Implantation and Lift-Off

Yixiong Zheng[1], Zixuan Feng[2], A F M Anhar Uddin Bhuiyan[2], Lingyu Meng[2], Samyak Dhole[1], Quanxi Jia[1], Hongping Zhao[2,3], Jung-Hun Seo[1, a)]

[1]Department of Materials Design and Innovation, University at Buffalo, The State University of New York, Buffalo, NY USA 14260

[2]Depertment of Electrical and Computer Engineering, The Ohio State University, Columbus, Ohio 43210, USA

[3]Department of Materials Science and Engineering, The Ohio State University, Columbus, Ohio 43210, USA

[a)]Author to whom correspondence should be addressed: junghuns@buffalo.edu

Abstract

In this paper, we have demonstrated the large-size free-standing single-crystal β-Ga₂O₃ NMs fabricated by the hydrogen implantation and lift-off process directly from MOCVD grown β-Ga₂O₃ epifilms on native substrates. The optimum implantation conditions were simulated with a Monte-Carlo simulation to obtain the high hydrogen concentration with a narrow ion distribution at the desired depth. Two as grown β-Ga₂O₃ samples with different orientation ([100] and [001]) were used and successfully create 1.2 μm thick β-Ga₂O₃ NMs without any physical damages. These β-Ga₂O₃ NMs were then transfer-printed onto rigid and flexible substrates such as SiC substrate and polyimide substrate. Various material characterizations were performed to investigate the crystal quality, surface morphology, optical property, mechanical property, and bandgap before and after the lift-off and revealed that good material quality is maintained. This result offers several benefits in that the thickness, doping, and size of β-Ga₂O₃ NMs can be fully controlled. Moreover, more advanced β-Ga₂O₃-based NM structures such as (Al$_x$Ga$_{1-x}$)₂O₃/Ga₂O₃ heterostructure NMs can be directly created from their bulk epitaxy substrates thus this result provides a viable route for the realization of high performance β-Ga₂O₃ NM-based electronics and optoelectronics that can be built on various substrates and platforms.

Beta-phase gallium oxide (β-Ga$_2$O$_3$) has attracted much attention as a promising wide bandgap semiconductor candidate due to its large bandgap with a high breakdown field and decent electron mobility.[1-4] The availability of large-size high-quality single-crystalline β-Ga$_2$O$_3$ native substrate and epitaxy layer via well-known substrate growth techniques such as the Czochralski method[5] and the Float Zone method[6] or by thin-film growth techniques such as molecular beam epitaxy (MBE)[7], metal-organic chemical vapor deposition (MOCVD)[8, 9], and halide vapor phase epitaxy (HVPE)[10] enable various large-scale high-performance electronics and optoelectronic applications.[11-14] Besides these advantageous material properties, β-Ga$_2$O$_3$ can also be mechanically exfoliated into a thin layer of β-Ga$_2$O$_3$ due to their different bonding strengths between [100] direction and other crystal orientations that associated with a monoclinic crystal structure. Thus, thin single-crystal β-Ga$_2$O$_3$ layers, also called β-Ga$_2$O$_3$ nanomembranes (NMs), can be produced directly from the bulk β-Ga$_2$O$_3$ substrate by a mechanical exfoliation method.[15-18] A free-standing form of β-Ga$_2$O$_3$ NM offers a new route to realize unique structures or device applications because it can be simply transfer-printed onto any desired substrates and form unique heterostructures or novel flexible electronics.[19, 20] For example, heterogeneous integration of transfer-printed β-Ga$_2$O$_3$ NMs onto a diamond substrate can be used to dissipate heat from β-Ga$_2$O$_3$ to compensate for the poor thermal property of β-Ga$_2$O$_3$ or novel heterojunctions.[21-23] Transfer-printed β-Ga$_2$O$_3$ NMs have also been used to realize flexible high-power switching devices or flexible solar-blind photodetectors that exhibited a comparable performance with that of their bulk counterparts. [24-26] However, one critical drawback is that β-Ga$_2$O$_3$ NMs are always cleaved at 77º angle to [201] direction when it is mechanically exfoliated due to the monoclinic crystal structure of β-Ga$_2$O$_3$ with a 103º angle. Therefore, the shape of the exfoliated β-Ga$_2$O$_3$ NM is always narrow and long. Our recent study also revealed that a wider β-Ga$_2$O$_3$ NMs leads to a thicker β-Ga$_2$O$_3$ NM.[26] For example, a 10 nm- and a 600 nm- thick β-Ga$_2$O$_3$ NMs typically show a width of 5 ~ 6 μm and 20 ~ 30 μm, respectively. In addition, it is difficult to precisely control a thickness of β-Ga$_2$O$_3$ NMs because the thickness can only be roughly controlled by the number of mechanical exfoliation steps. Another issue also related to the cleavage angle of β-Ga$_2$O$_3$ is that it is nearly impossible to create β-Ga$_2$O$_3$ NMs that have vertically grown multi-epitaxy layers, because all β-Ga$_2$O$_3$ NMs are exfoliated at a certain angle from the surface; thus severely limits the creation of functional β-Ga$_2$O$_3$ NM such as (Al$_x$Ga$_{1-x}$)$_2$O$_3$/Ga$_2$O$_3$ heterostructure NMs for various advanced electronics and optoelectronic applications.

In this paper, we demonstrated a large-size free-standing single-crystal β-Ga$_2$O$_3$ NMs fabricated by hydrogen implantation and lift-off directly from MOCVD grown epitaxy β-Ga$_2$O$_3$ samples. The use of hydrogen ions not only minimizes the crystal damage during ion implantation due to their light and small volume but also enables us to effectively separate the top portion of β-Ga$_2$O$_3$ from the substrate. Different implantation conditions were simulated with a Monte-Carlo simulation using a Silvaco Victory 2D Process simulator to obtain the high hydrogen concentration with a narrow ion distribution at a desired depth. Two β-Ga$_2$O$_3$ source wafers that were grown on

different crystal orientations ([100] and [001]) were used and successfully create 1.2 µm thick β-Ga_2O_3 NMs without any physical damages. These β-Ga_2O_3 NMs were then successfully transfer-printed onto rigid and flexible substrates such as SiC substrate and polyimide substrate. Various material characterizations were performed to investigate the crystal quality, surface morphology, optical property, mechanical property, and bandgap before and after the separation and revealed that no noticeable differences were observed. This result offers several benefits in that the thickness and size of β-Ga_2O_3 NMs can be accurately controlled as opposed to the narrow stripe-shaped β-Ga_2O_3 NMs from the uncontrolled conventional mechanical exfoliation method. Moreover, β-Ga_2O_3 NM-based functional free-standing semiconductor NMs such as $(Al_xGa_{1-x})_2O_3/Ga_2O_3$ heterostructure NMs can be directly created from their original hetero-epitaxy wafers without being restricted by their dimensional factors and easily integrated with any platform. Thus, this result provides a viable route to high performance β-Ga_2O_3 NM-based electronics and optoelectronics that can be built on various substrates such as flexible plastic or metallic substrates or different semiconductor platforms.

Figure 1(a) shows the schematic illustration of the β-Ga_2O_3 NM separation process. In this experiment, two 500 µm thick Fe doped β-Ga_2O_3 substrates (Novel Crystal Technology Inc.) with different orientations ([100] and [001]) and a Fe concentration of 1×10^{19} cm^{-3} were used. On top of these substrates, a 200 nm thick unintentionally doped homoepitaxy β-Ga_2O_3 thin-film grown by metalorganic chemical vapor deposition (MOCVD) as depicted in **Figure 1(a)(i)**. The detail of the samples can be found in **Figure S1** of Supplementary Information. The separation process starts with the hydrogen ion implantation (**Figure 1(a)(i)-(ii)**). Prior to the ion implantation, both samples were thoroughly cleaned with acetone, isopropyl alcohol, and deionized water with mild sonification. The detail of the ion implantation condition will be discussed in below related to **Figure 3**. In this experiment, the hydrogen implantation was performed with an energy of 190 keV and a dose of 2×10^{16} cm^2 to produce the dense hydrogen layer 1.2 µm underneath the wafer surface. The sample was then annealed at 250 °C for 24 hours to activate implanted hydrogen ions (**Figure 1(a)(iii)**). As implanted hydrogen ions reacted and became hydrogen gas (hydrogen micro-bubbles), the top portion of β-Ga_2O_3 was gradually separated from the substrate. This thin β-Ga_2O_3 can be now called β-Ga_2O_3 NM and gently registered on the β-Ga_2O_3 substrate without moving as shown in **Figure 1(a)(iv)**. Then, as depicted in **Figure 1(a)(v)-(viii)**, β-Ga_2O_3 NMs were transfer-printed onto rigid and flexible substrates using an elastomeric stamp (poly(dimethylsiloxane) (PDMS)) to construct the final structure, namely, β-Ga_2O_3 NMs on a foreign substrate (**Figure 1(a)(viii)**). The detail of the transfer printing process can be found elsewhere[27, 28]. In this experiment, the SiC and the polyimide substrates were used to represent rigid and flexible form of foreign substrate, but β-Ga_2O_3 NMs can be transfer-printed onto any type of rigid or flexible substrates. **Figure 1(b)** shows multiple images of 15 mm × 10 mm size single piece β-Ga_2O_3 NM on a PDMS stamp with three different magnifications to show the detail of the lifted-off β-Ga_2O_3 NM. **Figure 2(a)** shows a three-dimensional surface profile of β-Ga_2O_3 NM on the PDMS surface

taken after lifting up using Profilm3D Filmetric surface profiler. The surface profile image scanned ~500 μm^2 area with a spatial resolution of < 5 nm. **Figure 2(b)** shows the two-dimensional depth profile between the "A" and "B" points of **Figure 2(a)**, indicating that the surface of β-Ga$_2$O$_3$ NM is smooth and uniform. **Figure 2(c)** shows that the thickness of β-Ga$_2$O$_3$ NMs was measured to be 1.2 μm, and the surface roughness of 1.8 nm which is the same as the surface roughness of the β-Ga$_2$O$_3$ epifilms before the lift-off. The angled scanning electron microscopy (SEM) images (**Figure 2(c)**) also show that the surface is smooth without any cracks or fractures. These imaging results confirm that the layer separation occurred exactly at the depth as originally designed.

The process design for hydrogen implantation is a critical and most important step that determines a thickness of β-Ga$_2$O$_3$ NM after the lift-off process. The implantation modeling was performed using an ion implantation module of the Silvaco Victory 2D Process simulator to accurately predict the hydrogen distribution in the bulk β-Ga$_2$O$_3$ substrate. The hydrogen profile was modeled based on a Monte-Carlo method with 32000 hydrogen ions using an implantation energy ranging from 70 keV to 300 keV with a fixed dose at 2×10^{16} cm^{-2}. In each hydrogen implantation profile, we captured the depth where the hydrogen concentration exceeds mid-10^{20} cm^{-3}, because the layer separation will occur at this depth, thus the thickness of β-Ga$_2$O$_3$ NM after the lift-off process can be estimated. **Figure 3(a)** shows the summary data showing a predicted thickness of the separated β-Ga$_2$O$_3$ NMs as a function of different implantation energy with a fixed dose of 2×10^{16} cm^{-2}. A linear relationship between β-Ga$_2$O$_3$ NM thickness and implantation energy was observed as predicted by the energy (E) and projected range (R) relationship in the ion implantation theory: $R = \frac{1}{N} \int_0^E dE / S(E)$, where N is the number of ions per unit volume.[29]

Therefore, it is possible to accurately control the separation depth by controlling the implantation energy. In fact, this hydrogen implantation and layer-separation process is similar to the well-known SMART-CUT process, in that a dense hydrogen layer is used to separate the layer from the bulk substrate to fabricate various XOI (Semiconductor X-On Insulator) wafers such as SOI, GeOI, SiCOI and etc. [20, 30-32] Thus this hydrogen implantation and layer-separation process is a highly reliable process. **Figure 3(b)** shows the modeled hydrogen profile that is used in this experiment. According to this simulation result, the hydrogen implantation process with the energy of 190 keV and a dose of 2×10^{16} cm^2 yield a 1 μm thick β-Ga$_2$O$_3$ NM. The excessively high energy and dose level compared with the lift-off process for other materials are responsible for the high material density of β-Ga$_2$O$_3$.[30, 31] It should be noted that the hydrogen concentration at the separation region needs to be greater than 1×10^{20} cm^{-3} to create microbubbles for the layer lift-off without any cracks or fractures, because the failure to achieve dense hydrogen bubbles results in the partial layer separation and causes defects and cracks in β-Ga$_2$O$_3$ NMs. The star mark in **Figure 3(a) and (b)** indicate the actual thickness of β-Ga$_2$O$_3$ NM (~1.2 μm) after the lift-off process which agrees well with the predicted value. In this experiment, we designed a 1.2 μm thick β-Ga$_2$O$_3$ NM for the

proof of concept, but a wide range of β-Ga₂O₃ NM thicknesses (from a few hundreds of nm to several tens of μm range) can be realized by changing the hydrogen implantation condition.

Various material characterizations were exhibited to investigate differences before and after the layer lift-off process. In this characterization, β-Ga₂O₃ NM on the PDMS stamp which corresponds to the step (vi) in **Figure 1(a)** was used to avoid any possible material damages by the transfer-printing process that can affect the result. First, X-ray diffraction (XRD) measurements were performed to investigate the crystalline quality of lifted-off β-Ga₂O₃ NM using a PANalytical Empyrean X-ray diffractometer (Cu Kα radiation with operating voltage/current of 45 kV/40 mA) under ambient conditions with a 20–60° 2θ scattering angle range. As shown in **Figure 4(a) and (b)**, each XRD scan clearly indicates the peaks of [400], [600], and [800] planes for β-Ga₂O₃ NM from the [100]-oriented β-Ga₂O₃ substrate and [002] plane for β-Ga₂O₃ NM from the [001]-oriented β-Ga₂O₃ substrate. The full width at half maximum (FWHM) values of the most dominant XRD profiles from each sample, namely, [200] plane for the [100]-oriented β-Ga₂O₃ NM and [002] plane for the β-Ga₂O₃ NM, are measured to be 0.013° and 0.029°. (see **Figure S2** in Supplementary Information) These FWHM values and 2θ remain unchanged compared to their bulk counters (**Figure S3** in Supplementary Information) and it implies that the quality of lifted-off β-Ga₂O₃ NMs remain unchanged. We also compared the Raman spectrum from a bulk β-Ga₂O₃ to that of lifted-off β-Ga₂O₃ NMs using a Renishaw InVia Raman spectroscopy that was equipped with a 514 nm green laser and a ×50 objective lens. **Figure 4(c) and (d)** show the Raman spectra that were taken from the bulk β-Ga₂O₃ and lifted-off β-Ga₂O₃ NMs. The Raman intensity from the bulk β-Ga₂O₃ is much stronger than that of lifted-off β-Ga₂O₃ NM due to the difference in their physical thicknesses (500 μm vs. 1.2 μm). All Raman spectra present 11 typical Raman modes from 100 cm⁻¹ to 900 cm⁻¹ without any noticeable shifting indicating that the β-Ga₂O₃ NMs do not have any damage in the crystal structure and internal strain after the lift-off process compared to bulk β-Ga₂O₃. However, [100] β-Ga₂O₃ (both bulk and NM) has a stronger $A_{g,3}$ Raman mode (appeared at 200 cm⁻¹) and weaker $A_{g,10}$ Raman mode (appeared at 760 cm⁻¹) which indicates that the vibration modes of the Ga–O chain in the Ga_IO_4 tetrahedron have a dominant position in [100] β-Ga₂O₃ compared with [001] β-Ga₂O₃. Interestingly, the $A_{g,10}$ Raman mode becomes significantly weaker in both [100] and [001] β-Ga₂O₃ NMs. The $A_{g,10}$ Raman mode is ascribed to the combination of the symmetrical stretching vibration of the $Ga_I(O_I\text{-}O_{III})$ bond of the Ga_IO_4 unit and the bending vibration of the $Ga_I(O_{II})_2$ bond and this mode is affected by the adjacent octahedron.[33] The Fe dopants in bulk β-Ga₂O₃ typically replace GaII atoms in the center of $Ga_{II}O_6$ octahedron, therefore the $A_{g,10}$ Raman mode in bulk β-Ga₂O₃ tends to be very strong. On the contrary, undoped β-Ga₂O₃ has a weaker $A_{g,10}$ Raman mode as a result of lower dopant concentrations.[34] In β-Ga₂O₃ NMs, the relative thickness of Fe doped β-Ga₂O₃ in β-Ga₂O₃ NM is reduced from 500 μm to 0.9 μm after the lift-off process. Therefore, the relative $A_{g,10}$ Raman mode vibration is also noticeably reduced both in [100] and [001] β-Ga₂O₃ NMs. **Figure 5** shows Raman

spectra taken after transfer-printing [001]-oriented β-Ga$_2$O$_3$ NMs onto a SiC and polyimide substrates. As shown in **Figure 5(a)**, the β-Ga$_2$O$_3$ NM on SiC substrate clearly presents 11 β-Ga$_2$O$_3$ characteristic modes as well as SiC peaks at 780 nm and 980 nm respectively without any peak shifting, suggesting that β-Ga$_2$O$_3$ NM does not suffer from any residual stress. Also, the similar phenomenon was measured from β-Ga$_2$O$_3$ NM on polyimide structure that no noticeable peak shifting was observed as shown in **Figure 5(b)**. Therefore, the lifted β-Ga$_2$O$_3$ NMs did not experience any strain or material degradation during the lift-off process and the integration on the foreign substrate. After we confirmed the crystal quality of the transferred β-Ga$_2$O$_3$ NMs, we performed a strain-Raman spectral study to investigate Raman shifts under different uniaxial strain conditions. In order to accurately measure the changes in the Raman spectrum under the uniaxial strain condition, we employed convex and concave molds that have different curve radii ranging from 110 mm to 20 mm which corresponds to the uniaxial strains up to 0.32 % of the tensile strain (for the convex mold) and up to 0.19 % of the compressive strain (for the concave mold). The most dominant peak A$_{g,3}$ peak at 200.4 cm^{-1} was chosen to trace the strain-dependent characteristics. As shown in **Figure 5(c), Figure S4, and Figure S5**, the peak shifting value of A$_{g,3}$ was measured to be 2.56 cm^{-1} /Δε. This value is larger than typical 2D transition metal dichalcogenide (TMD) semiconductors[35], but similar to other single crystal semiconductor NMs[36].

To further investigate the impact of the hydrogen implantation and lift-off process on the optical property and bandgap of β-Ga$_2$O$_3$ NM, the optical property characterization was performed. Firstly, the refractive index (*n*) and extinction coefficient (*k*) were measured at the wavelength from 200 nm to 400 nm using a customized UV-to-visible spectrometer. As shown in **Figure 6(a) and (b)**, *n* and *k* values for bulk β-Ga$_2$O$_3$ and β-Ga$_2$O$_3$NMs of both [100] and [001] orientations on SiC substrates were compared. Both n and k values are very similar between the bulk format and NM format of β-Ga$_2$O$_3$. The small difference is probably attributed to the light reflection from the different substrates (β-Ga$_2$O$_3$ substrate vs. SiC substrate) and the slight difference in doping concentration of bulk β-Ga$_2$O$_3$ and β-Ga$_2$O$_3$ NM. Using these measured n and k values, the absorption coefficient can be obtained from the extinction coefficient using the following equation: $\alpha(\lambda)=[2\pi \cdot k(\lambda)]/\lambda$ by the complex index of refraction ($N = n - ik$) relationship.[37] Then, the optical bandgap for the direct electron transition can be calculated using the Tauc plot formula: $\alpha \cdot h \cdot v = C(h \cdot v - E_g)^{\wedge(1/2)}$, where $h \cdot v$ is the photon energy, λ is the wavelength and C is a constant.[37] From the Tauc plot, the bandgap (E_g) could be estimated by extrapolating the linear sections to the axis of energy ($h \cdot v$). **Figure 6(c)** shows the estimated bandgap of bulk β-Ga$_2$O$_3$ and β-Ga$_2$O$_3$NMs of both [100] and [001] orientations. Interestingly, while the bandgap values of bulk [100] and [001] β-Ga$_2$O$_3$ are calculated to be 4.94 eV and 4.93 eV, the bandgap values of [100] and [001] β-Ga$_2$O$_3$ NMs are slightly decreased to be 4.94 eV and 4.88 eV, respectively. Although the difference in bandgap between the bulk β-Ga$_2$O$_3$ substrate and β-Ga$_2$O$_3$NM is about 0.2~0.3 eV, this difference can be explained by the total amount of dopants in bulk β-Ga$_2$O$_3$ substrate β-Ga$_2$O$_3$ NMs. Rafique et al. reported that a 100 times difference in doping concentration (~10^{17} cm^{-3} vs

~10^{19} cm^{-3}) can result in ~1 % difference in bandgap of β-Ga$_2$O$_3$.[38] In fact, a few meV bandgap reduction by decreasing doping concentration is commonly observed in a similar material system such as GaAs and GaN.[39, 40] In our case, as depicted in **Figure 1(a)**, a 500 μm thick β-Ga$_2$O$_3$ substrate contains Fe dopants with a concentration of 1×10^{19} cm^{-3}, while the top 200 nm epitaxy layer has an unintentional doping concentration of $< 1 \times 10^{16}$ cm^{-3}. When the bandgap of bulk β-Ga$_2$O$_3$ is measured, the effect on optical parameters by a 200 nm thick UID epitaxy β-Ga$_2$O$_3$ NM is almost negligible compared with that of 500 μm thick Fe-doped β-Ga$_2$O$_3$ substrate. However, when the optical parameters of β-Ga$_2$O$_3$ NM are measured, the 200 nm thick UID epitaxy β-Ga$_2$O$_3$ NM cannot be negligible, because the thickness of Fe-doped β-Ga$_2$O$_3$ is estimated to be ~900 nm. Therefore, the difference in bandgap is not by the hydrogen implantation and lift-off process, but by the relative thickness ratio between the Fe-doped bulk β-Ga$_2$O$_3$ and β-Ga$_2$O$_3$ NM, because the effect of the dopants becomes more dominant in β-Ga$_2$O$_3$ NMs

In conclusion, we have successfully demonstrated the large-size free-standing single-crystal β-Ga$_2$O$_3$ NMs fabricated by the hydrogen implantation and lift-off process directly from MOCVD grown β-Ga$_2$O$_3$ substrates. The optimum implantation conditions were simulated with a Monte-Carlo method to obtain the high hydrogen concentration with a narrow ion distribution at the desired depth. Two β-Ga$_2$O$_3$ source wafers with different orientations (i.e., [100]- and [001]-oriented β-Ga$_2$O$_3$ substrates) were used and successfully create 1.2 μm thick β-Ga$_2$O$_3$ NMs without any physical damages. These β-Ga$_2$O$_3$ NMs were then transfer-printed onto rigid and flexible substrates such as SiC substrate and polyimide substrate. Various material characterizations were performed to investigate the crystal quality, surface morphology, optical property, mechanical property, and bandgap before and after the separation and revealed that good material quality was maintained. This result offers several benefits in that the thickness and size of β-Ga$_2$O$_3$ NMs can be fully controlled. Moreover, more advanced β-Ga$_2$O$_3$ NM structures such as (Al$_x$Ga$_{1-x}$)$_2$O$_3$/Ga$_2$O$_3$ heterostructure NMs can be directly created from their bulk epitaxy wafers. Several following studies need to be conducted such as the impact of growth conditions such as growth temperature and n-type/p-type doping concentration on the surface roughness, defect density of the bulk source β-Ga$_2$O$_3$ to create the uniform and high-quality β-Ga$_2$O$_3$ NMs. Nevertheless, this result provides a viable route for the realization of high-performance β-Ga$_2$O$_3$ NM-based electronics and optoelectronics that can be built on various substrates and platforms.

ACKNOWLEDGEMENT
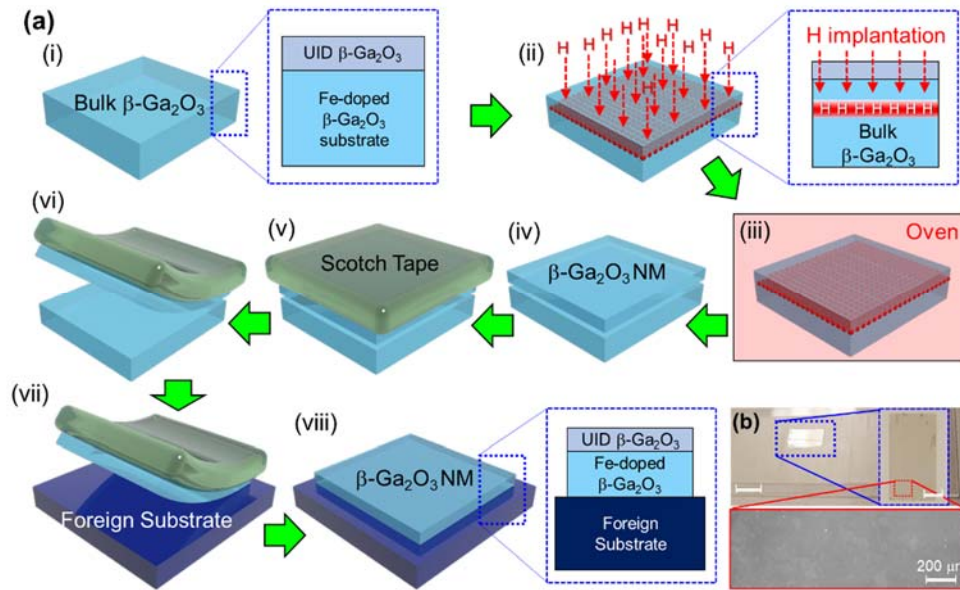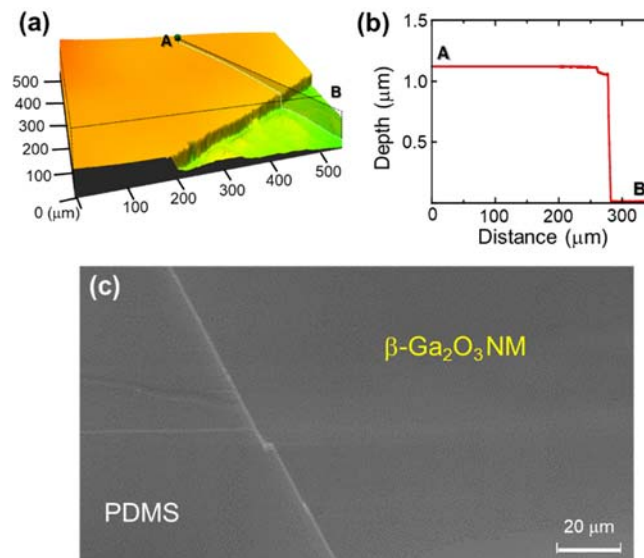
CONFLICTS OF INTEREST

There are no conflicts to declare.

Figure 1. (a) a schematic illustration of the β-Ga₂O₃ lift-off process, **(b)** images of lifted β-Ga₂O₃ in different magnifications (upper left) x2, (upper right) x5, (bottom) x 400. Scale bars in upper left and right images are 10mm and 5mm respectively.


Figure 2. (a) three dimensional surface morphology of β-Ga₂O₃ NM and **(b)** two-dimensional depth profile between the point A and B in Figure 2(a), **(c)** an angled SEM image of β-Ga₂O₃ NM taken on a PDMS stamp.
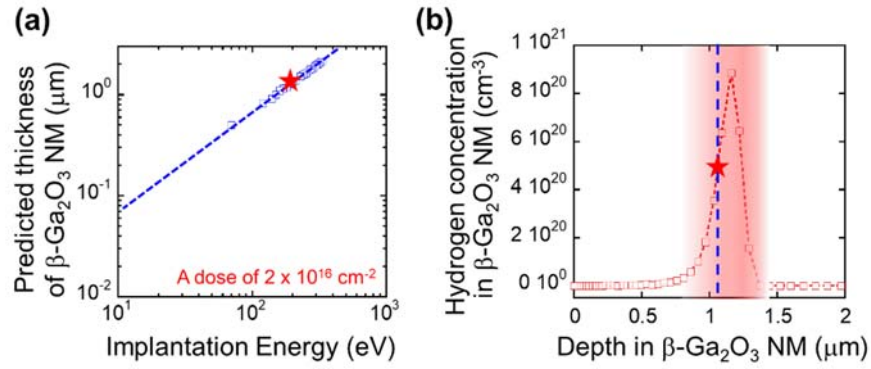
Figure 3. (a) a predicted thickness of β-Ga₂O₃ NM with respect to various implantation energy from 70 eV to 300 eV. **(b)** a simulated hydrogen concentration profile in β-Ga₂O₃ NM. A star mark in each figure denotes the actual thickness of β-Ga₂O₃ NM.
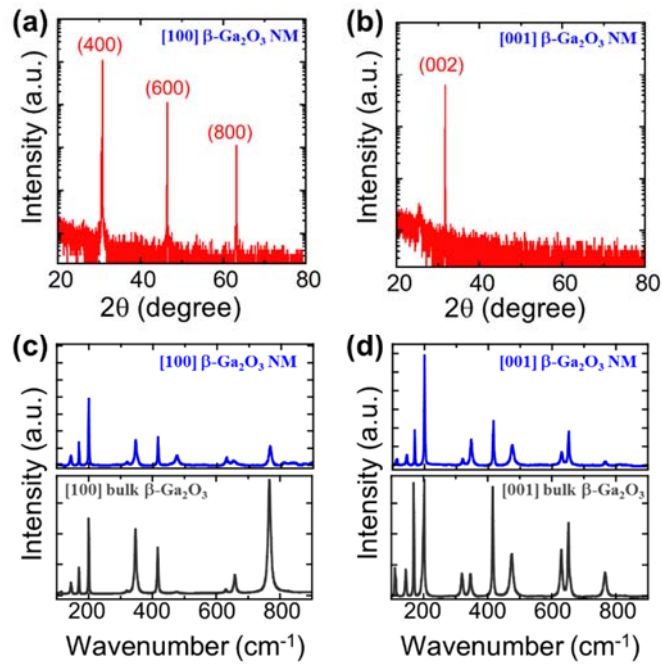
Figure 4. Measured XRD spectrum from **(a)** [100]-oriented β-Ga₂O₃ NM and **(b)** [001]-oriented β-Ga₂O₃ NM. Measured Raman spectrum from **(c)** [100]-oriented β-Ga₂O₃ NM and **(d)** [001]-oriented β-Ga₂O₃ NM compared with their bulk form of substrates (lower panel of Figure 4(c) and (d)).
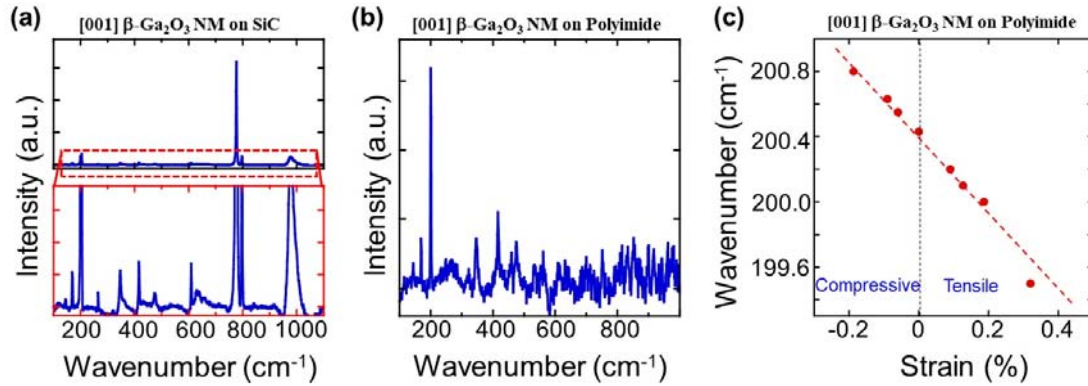
Figure 5. Measured Raman spectrum from [001]-oriented β-Ga₂O₃ NM transferred on SiC substrate. A bottom section of the plot shows the zoomed-in view of the Raman spectrum and **(b)** Measured Raman spectrum from [001]-oriented β-Ga₂O₃ NM transferred on on polyimide substrate. **(c)** Measured $A_{g,3}$ Raman modes as a function of applied strain from 0.19% of the tensile strain to 0.32 % of the compressive strain.
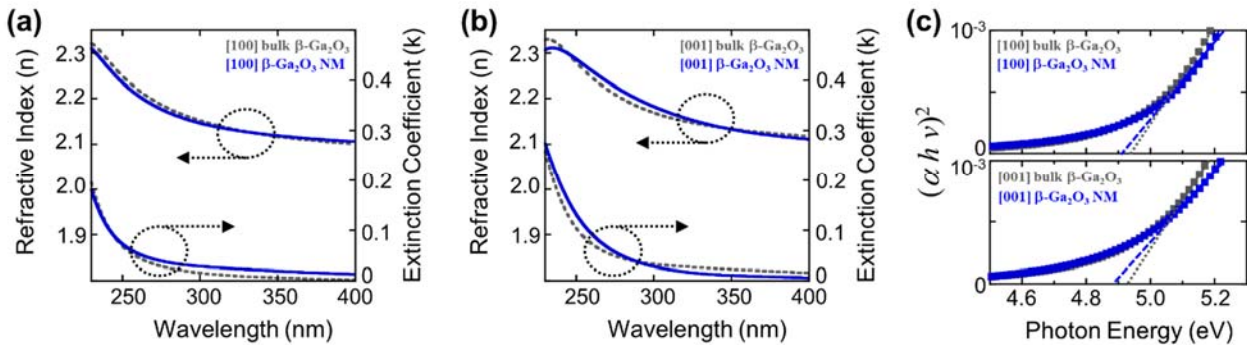
Figure 6. Measured optical properties: (left axis) refractive index (*n*) and (right axis) extinction coefficient (*k*) of **(a)** [100]-oriented β-Ga₂O₃ NM and **(b)** [001]-oriented β-Ga₂O₃ NM compared with their bulk form of substrates. **(c)** extracted bandgap of (upper) [100]-oriented β-Ga₂O₃ NM and (lower) [001]-oriented β-Ga₂O₃ NM compared with their bulk form of substrates.

REFERENCES

1. N. Ma, N. Tanen, A. Verma, Z. Guo, T. Luo, H. Xing and D. Jena, *Applied Physics Letters*, 2016, **109**, 212101.
2. M. Higashiwaki, K. Sasaki, A. Kuramata, T. Masui and S. Yamakoshi, *Applied Physics Letters*, 2012, **100**, 013504.
3. S. Sharma, K. Zeng, S. Saha and U. Singisetti, *IEEE Electron Device Letters*, 2020, **41**, 836-839.
4. E. Swinnich, Y. J. Dave, E. B. Pitman, S. Broderick, B. Mazumder and J.-H. Seo, *Materials Discovery*, 2018, **11**, 1-5.
5. Y. Tomm, P. Reiche, D. Klimm and T. Fukuda, *Journal of crystal growth*, 2000, **220**, 510-514.
6. Y. Tomm, J. Ko, A. Yoshikawa and T. Fukuda, *Solar energy materials and solar cells*, 2001, **66**, 369-374.
7. K. Sasaki, M. Higashiwaki, A. Kuramata, T. Masui and S. Yamakoshi, *Journal of Crystal Growth*, 2013, **378**, 591-595.
8. Z. Feng, A. F. M. A. U. Bhuiyan, M. R. Karim and H. Zhao, *Applied Physics Letters*, 2019, **114**, 250601.
9. Z. Feng, A. F. M. A. U. Bhuiyan, Z. Xia, W. Moore, Z. Chen, J. F. McGlone, D. R. Daughton, A. R. Arehart, S. A. Ringel, S. Rajan and H. Zhao, *physica status solidi (RRL) – Rapid Research Letters*, 2020, **14**, 2000145.
10. H. Murakami, K. Nomura, K. Goto, K. Sasaki, K. Kawara, Q. T. Thieu, R. Togashi, Y. Kumagai, M. Higashiwaki, A. Kuramata, S. Yamakoshi, B. Monemar and A. Koukitu, *Applied Physics Express*, 2014, **8**, 015503.
11. S. Oh, C.-K. Kim and J. Kim, *Acs Photonics*, 2017, **5**, 1123-1128.
12. M. Higashiwaki, K. Sasaki, T. Kamimura, M. Hoi Wong, D. Krishnamurthy, A. Kuramata, T. Masui and S. Yamakoshi, *Applied Physics Letters*, 2013, **103**, 123511.
13. A. J. Green, K. D. Chabak, M. Baldini, N. Moser, R. Gilbert, R. C. Fitch, G. Wagner, Z. Galazka, J. Mccandless and A. Crespo, *IEEE Electron Device Letters*, 2017, **38**, 790-793.
14. M. Higashiwaki, K. Sasaki, H. Murakami, Y. Kumagai, A. Koukitu, A. Kuramata, T. Masui and S. Yamakoshi, *Semiconductor Science and Technology*, 2016, **31**, 034001.
15. H. Zhou, M. Si, S. Alghamdi, G. Qiu, L. Yang and P. D. Ye, *IEEE Electron Device Letters*, 2017, **38**, 103-106.
16. X. Yan, I. S. Esqueda, J. Ma, J. Tice and H. Wang, *Applied Physics Letters*, 2018, **112**, 032101.
17. S. Oh, M. A. Mastro, M. J. Tadjer and J. Kim, *ECS Journal of Solid State Science and Technology*, 2017, **6**, Q79.
18. J. Montes, C. Yang, H. Fu, T.-H. Yang, K. Fu, H. Chen, J. Zhou, X. Huang and Y. Zhao, *Applied Physics Letters*, 2019, **114**, 162103.
19. J.-H. Seo, E. Swinnich, Y.-Y. Zhang and M. Kim, *Materials Research Letters*, 2020, **8**, 123-144.
20. M. Kim, J.-H. Seo, U. Singisetti and Z. Ma, *Journal of Materials Chemistry C*, 2017, **5**, 8338-8354.
21. Y. Zheng and J.-H. Seo, *Nano Express*, 2020, **1**, 030010.
22. Y. Zheng, E. Swinnich and J.-H. Seo, *ECS Journal of Solid State Science and Technology*, 2020, **9**, 055007.

23. H. Kim, S. Tarelkin, A. Polyakov, S. Troschiev, S. Nosukhin, M. Kuznetsov and J. Kim, *ECS Journal of Solid State Science and Technology*, 2020, **9**, 045004.
24. M. N. Hasan, J. Lai, E. Swinnich, Y. Zheng, B. S. Baboukani, P. C. Nalam and J. H. Seo, *Advanced Electronic Materials*, 2020, 2000763.
25. J. Lai, M. N. Hasan, E. Swinnich, Z. Tang, S.-H. Shin, M. Kim, P. Zhang and J.-H. Seo, *Journal of Materials Chemistry C*, 2020, **8**, 14732-14739.
26. E. Swinnich, M. N. Hasan, K. Zeng, Y. Dove, U. Singisetti, B. Mazumder and J. H. Seo, *Advanced Electronic Materials*, 2019, **5**, 1800714.
27. H. Yang, D. Zhao, S. Chuwongin, J.-H. Seo, W. Yang, Y. Shuai, J. Berggren, M. Hammar, Z. Ma and W. Zhou, *Nature Photonics*, 2012, **6**, 615-620.
28. J.-H. Seo, K. Zhang, M. Kim, W. Zhou and Z. Ma, *NPJ Flexible Electronics*, 2017, **1**, 1-7.
29. J. F. Gibbons, *Proceedings of the IEEE*, 1968, **56**, 295-319.
30. M. Kim, J.-H. Seo, D. Zhao, S.-C. Liu, K. Kim, K. Lim, W. Zhou, E. Waks and Z. Ma, *Journal of Materials Chemistry C*, 2017, **5**, 264-268.
31. M. Kim, S.-C. Liu, T. J. Kim, J. Lee, J.-H. Seo, W. Zhou and Z. Ma, *Optics express*, 2016, **24**, 16894-16903.
32. J.-H. Seo, T.-H. Chang, J. Lee, R. Sabo, W. Zhou, Z. Cai, S. Gong and Z. Ma, *Applied Physics Letters*, 2015, **106**, 262101.
33. S. Siah, R. Brandt, K. Lim, L. Schelhas, R. Jaramillo, M. Heinemann, D. Chua, J. Wright, J. D. Perkins and C. Segre, *Applied Physics Letters*, 2015, **107**, 252103.
34. K. Zhang, Z. Xu, S. Zhang, H. Wang, H. Cheng, J. Hao, J. Wu and F. Fang, *Physica B: Condensed Matter*, 2021, **600**, 412624.
35. S. Liang, M. N. Hasan and J.-H. Seo, *Nanomaterials*, 2019, **9**, 566.
36. M. Kim, H. Mi, M. Cho, J.-H. Seo, W. Zhou, S. Gong and Z. Ma, *Applied Physics Letters*, 2015, **106**, 212107.
37. A. Forouhi and I. Bloomer, *Physical review B*, 1988, **38**, 1865.
38. S. Rafique, L. Han, S. Mou and H. Zhao, *Opt. Mater. Express*, 2017, **7**, 3561-3570.
39. J. Piprek, in *Semiconductor Optoelectronic Devices*, ed. J. Piprek, Academic Press, Boston, 2003, DOI: https://doi.org/10.1016/B978-0-08-046978-2.50027-2, pp. 13-48.
40. Y. Zhang, A. Mascarenhas, H. Xin and C. Tu, *Physical Review B*, 2001, **63**, 161303.